

Testing Munk’s hypothesis for submesoscale eddy generation using observations in the North Atlantic

Christian E. Buckingham^{1*}, Zammath Khaleel^{1†}, Ayah Lazar^{2‡}, Adrian P. Martin³, John T. Allen^{4,5}, Alberto C. Naveira Garabato¹, Andrew F. Thompson² and Clément Vic¹

¹University of Southampton, National Oceanography Centre, Southampton, United Kingdom

²California Institute of Technology, Pasadena, California, United States

³National Oceanography Centre, Southampton, United Kingdom

⁴University of Portsmouth, Portsmouth, United Kingdom

⁵VECTis Environmental Consultants, LLP, Portsmouth, United Kingdom

Contents

1. Text 1 to 5
2. Figures 1 to 5
3. Table 1

Introduction

Below, we provide supporting material. This includes example imagery during this period, clear-sky occurrences during the entire OSMOSIS period, evidence for connections (albeit speculative) to spiral eddies documented by *Scully-Power* [1986]; *Munk et al.* [2000], errors resulting from optimal interpolation of SeaSoar II measurements and estimates of the lateral shear across the front.

1 Clear-sky occurrences (September 2012–September 2013)

As mentioned in the manuscript, we provide a list of periods classified as clear-sky according to our definition *and* which exceed two hours in duration (Table 1). We believe this may help in future analysis of the OSMOSIS record. Note: not all imagery obtained during these periods resulted in stellar imagery. Considerable information might be teased out by using more sophisticated processing in concert with geosynchronous data. Another option might be to identify coverage from the MODIS sensor onboard the Aqua spacecraft. This sensor has a spatial resolution near ~ 1 km and would complement these data considerably. Another thing to note is that the visible portion of the electromagnetic spectrum on both the VIIRS and MODIS instruments provides information about chlorophyll concentration. Thus, consideration of an additional sensor could increase the chances of obtaining coincident chlorophyll and *in situ* (i.e., mooring- and glider-based) measurements. In summary, these clear-sky periods may be beneficial to the reader.

2 Additional infrared imagery

Figure 1 provides several example SST images obtained from cross-referencing clear-sky conditions with VIIRS onboard Suomi-NPP. Two examples are highlighted. One of these is the unstable front described in the main manuscript on 19 September 2012 (first row, second column). The second pertains to upwelling of waters within an anticyclonic mesoscale eddy west of the observation site during July and August 2013 (e.g., 12 July 2012; fourth row, third

*Current address: British Antarctic Survey, Cambridge, United Kingdom

†Current address: Ministry of Environment and Energy, Malé, Maldives

‡Current address: Israel Oceanographic and Limnological Research, Haifa, Israel

Corresponding author: C. E. Buckingham, c.e.buckingham@bas.ac.uk

column) and which may be evidence of symmetric instability within the mesoscale eddy [Branigan, 2016].

3 Spiral eddies in infrared measurements of sea surface temperature?

We stated within the manuscript that the occurrence of swirling vortices along the thermal front was most likely related to “spiral eddies” documented within optical images by *Scully-Power* [1986]; *Munk et al.* [2000]. Figure 2a illustrates an example of spiral eddies from the Apollo shuttle missions [Scully-Power, 1986]. Using image processing methods (e.g., morphological operations and normalization), we isolated tracer concentrations elevated above background levels. The resulting binary image is displayed in Figure 2b. Finally, we hand-drew contours of these tracers as objectively as possible, connecting previously unconnected segments (Figure 2c). The tracer contour has appearance that is similar to the SST contour separating warm and cool waters in the study. In summary, while we cannot state for certain that the observed SST image provides evidence of spiral eddies in SST, we suspect they are produced by the same underlying phenomenon.

4 Interpolation of SeaSoar II measurements

While useful for understanding the horizontal and vertical structure of ocean fronts, interpolation of discrete measurements from SeaSoar II yield density and velocity fields that are smoothed relative to true values. In particular, the lateral smoothing inherent in the Barnes analysis employed here [Barnes, 1964, 1994] may bias eddy scales obtained in the BTI analysis; its effect on the widths of the horizontally-sheared regions, a and b , is paramount.⁴ In order to quantify the lower bound for these quantities, we simulated a jet-like velocity field consisting of constant-vorticity sheets and conducted an optimal interpolation of these data. A comparison of original and processed fields is shown in Figure 3. For a jet-like profile having sheared widths $a' = b' = 8.3$ km, the result after the Barnes analysis is a Gaussian-like profile with widths $a = b = 20.0$ km. That is, the resulting jet has shear width approximately 2.4 times its original scale. We have rounded this to 3.0 to be conservative. Given our estimated shear widths of $a = 20.0$ and $b = 25.0$ km, this implies the true widths are no smaller than $a' = 6.7$ and $b' = 8.3$ km, respectively. Note, that the magnitude of the flow is reduced, as well. This suggests the unbiased shear parameter to use for the BTI model is larger: $U'_o \approx 2U_o = (2)(0.24)$ m/s = 0.48 m/s. We did not use this value within the text since this parameter modifies only the growth rate and not the scale of the most unstable mode. We did, however, use it to estimate the gradient Rossby number (below).

We emphasize that the shear widths obtained above are somewhat conservative. We have done this in order to be explicit about how the horizontal shear model used in the manuscript does not explain the observed eddy sizes. In reality, the true shear widths are likely closer to $20/2.5 = 8$ km.

5 Magnitude of lateral shear across the front

For completion, we document higher-order derivatives of the SeaSoar II data. In general, we are not confident of small-scale features observed in these quantities. This is because the errors arising during the interpolation scheme will tend to amplify when spatial gradients are taken. Nevertheless, the general magnitude of horizontal shear across the front should be well-represented by these estimates. Note: where other optimal interpolation schemes intro-

⁴ Note, the vertical scale is not affected in the same way since the averaging depth was minimal. As eddy scales under the BCI model depend heavily on the choice of H , these are not modified greatly. The lateral buoyancy gradient is relaxed, however, and this will tend to reduce growth rates relative to those reported here.

duce errors, we have minimized many of these by using the Barnes analysis [Barnes, 1964, 1994].

Figure 4 depicts the gradient Rossby number, $Ro = \zeta/f \approx -f^{-1}\partial\bar{u}/\partial y$, estimated from the SeaSoar II data. Note that amplitudes do not exceed 0.125. However, given the smoothing inherent in the interpolation scheme, we estimate lower and upper bounds on this value of 0.1–0.55. These bounds can be obtained as follows. We first subtract from the total current magnitude the background value to obtain $U_o = 0.24 \text{ m s}^{-1}$. For the upper bound, we multiply by 2 to obtain $U'_o = 2U_o \text{ m s}^{-1}$, whereas we retain U_o only for the lower bound. Finally, we divide by the product of f and the shear width, a . In this calculation, we used $a = 8.0 \text{ km}$ (upper bound) and $a = 20 \text{ km}$ (lower bound). [For example, for the upper bound, $|Ro| = f^{-1}(U'_o/a) = f^{-1}(0.48/8000) = 0.55$, where $f \approx 1.0940 \times 10^{-4} \text{ s}^{-1}$ and a is expressed in meters.]

For geophysical flows, a necessary but insufficient criterion for instability is that the cross-front gradient of potential vorticity, $\partial q/\partial y$, change sign somewhere within the flow. For baroclinic instability, this quantity will be dominated by the cross-front gradient of vertical shear, $\partial^2 \mathbf{u}/\partial z \partial y$, whereas for barotropic instability, it will be dominated by the cross-front gradient of relative vorticity, $\partial^2 u/\partial y^2$. In Figure 5, we depict the meridional (i.e., cross-front) gradient of potential vorticity, $q_y = \partial q/\partial y$. While interpretation of this graphic is beyond the scope of this study, we include it as supporting material since it suggests a two-dimensional instability analysis may be needed. Two features are suggested in this field. First, there is a large change in sign of q_y at the pycnocline (all cross-front distances, depths 40–50 m), reflecting the dominance of baroclinic instability. Second, there is a more subtle decrease in this quantity on the northward side of the front (cross-front distances 0–7 km, depths 0–30 m), reflecting the smaller but potential importance of barotropic shear on the northern side of the front. Note: as q_y is a second-order derivative, we encourage only qualitative interpretation of this graphic and have therefore provided it only as supporting material.

References

- Barnes, S. L. (1964), A technique for maximizing details in numerical weather map analysis, *Journal of Applied Meteorology*, 3(4), 396–409, doi:10.1175/1520-0450(1964)003<0396:ATFMDI>2.0.CO;2.
- Barnes, S. L. (1994), Applications of the Barnes objective analysis scheme. Part II: Improving derivative estimates, *Journal of Atmospheric and Oceanic Technology*, 11(6), 1449–1458.
- Brannigan, L. (2016), Intense submesoscale upwelling in anticyclonic eddies, *Geophysical Research Letters*, 43(7), 3360–3369, doi:10.1002/2016GL067926.
- Gonzalez, R. C., R. E. Woods, and S. L. Eddins (2004), *Digital image processing using MATLAB*, Pearson Education India.
- Munk, W., L. Armi, K. Fischer, and F. Zachariasen (2000), Spirals on the sea, in *Proceedings of the Royal Society of London A: Mathematical, Physical and Engineering Sciences*, vol. 456, pp. 1217–1280, The Royal Society.
- Scully-Power, P. (1986), Navy Oceanographer Shuttle observations, STS 41-G Mission Report, *Tech. rep.*, DTIC Document.

Table 1. Clear-sky occurrences exceeding 2 hours at the OSMOSIS mooring site and average fractional cloud cover (FCC) amongst all four small circles and within each period.

Start Time	End Time	\overline{FCC}
2012-09-01 03:00:00	2012-09-01 11:00:00	0.24
2012-09-05 21:00:00	2012-09-07 02:00:00	0.23
2012-09-13 23:00:00	2012-09-14 05:00:00	0.31
2012-09-15 19:00:00	2012-09-15 23:00:00	0.19
2012-09-18 20:00:00	2012-09-19 13:00:00	0.37
2012-09-21 08:00:00	2012-09-21 21:00:00	0.18
2012-09-28 15:00:00	2012-09-29 03:00:00	0.45
2012-10-21 11:00:00	2012-10-21 19:00:00	0.26
2012-10-23 22:00:00	2012-10-24 02:00:00	0.23
2012-11-19 04:00:00	2012-11-19 12:00:00	0.42
2012-11-21 00:00:00	2012-11-21 13:00:00	0.60
2012-12-17 10:00:00	2012-12-17 13:00:00	0.15
2012-12-18 22:00:00	2012-12-21 00:00:00	0.60
2012-12-25 14:00:00	2012-12-25 17:00:00	0.17
2013-01-07 23:00:00	2013-01-09 05:00:00	0.47
2013-01-25 13:00:00	2013-01-25 21:00:00	0.15
2013-01-29 23:00:00	2013-01-30 10:00:00	0.59
2013-02-07 13:00:00	2013-02-08 11:00:00	0.39
2013-02-13 21:00:00	2013-02-14 09:00:00	0.36
2013-02-17 19:00:00	2013-02-18 01:00:00	0.22
2013-02-18 18:00:00	2013-02-20 03:00:00	0.38
2013-02-21 01:00:00	2013-02-21 06:00:00	0.19
2013-02-22 06:00:00	2013-02-22 12:00:00	0.44
2013-03-25 00:00:00	2013-03-25 07:00:00	0.35
2013-03-28 22:00:00	2013-03-30 04:00:00	0.49
2013-03-30 21:00:00	2013-03-31 05:00:00	0.20
2013-04-01 22:00:00	2013-04-02 15:00:00	0.24
2013-04-12 02:00:00	2013-04-12 09:00:00	0.35
2013-04-14 14:00:00	2013-04-15 01:00:00	0.43
2013-04-18 09:00:00	2013-04-18 21:00:00	0.51
2013-04-19 15:00:00	2013-04-20 05:00:00	0.40
2013-04-30 11:00:00	2013-04-30 15:00:00	0.36
2013-05-04 15:00:00	2013-05-04 17:00:00	0.28
2013-05-12 04:00:00	2013-05-12 13:00:00	0.35
2013-05-31 19:00:00	2013-06-01 06:00:00	0.12
2013-06-02 16:00:00	2013-06-02 21:00:00	0.32
2013-06-03 14:00:00	2013-06-04 02:00:00	0.44
2013-06-12 19:00:00	2013-06-13 01:00:00	0.24
2013-06-14 07:00:00	2013-06-14 12:00:00	0.49
2013-06-18 21:00:00	2013-06-19 07:00:00	0.12
2013-06-28 20:00:00	2013-06-29 03:00:00	0.12
2013-07-04 00:00:00	2013-07-05 00:00:00	0.41
2013-07-05 14:00:00	2013-07-06 06:00:00	0.10
2013-07-07 00:00:00	2013-07-09 13:00:00	0.27
2013-07-10 04:00:00	2013-07-13 05:00:00	0.33
2013-07-16 16:00:00	2013-07-17 21:00:00	0.39
2013-07-18 19:00:00	2013-07-19 15:00:00	0.43
2013-07-22 21:00:00	2013-07-22 23:00:00	0.25
2013-08-05 00:00:00	2013-08-05 02:00:00	0.34
2013-08-19 15:00:00	2013-08-19 19:00:00	0.29
2013-08-21 13:00:00	2013-08-21 16:00:00	0.19
2013-08-22 21:00:00	2013-08-22 23:00:00	0.26
2013-08-27 21:00:00	2013-08-28 06:00:00	0.21
2013-08-29 18:00:00	2013-08-30 04:00:00	0.40
2013-08-31 15:00:00	2013-09-01 00:00:00	0.32

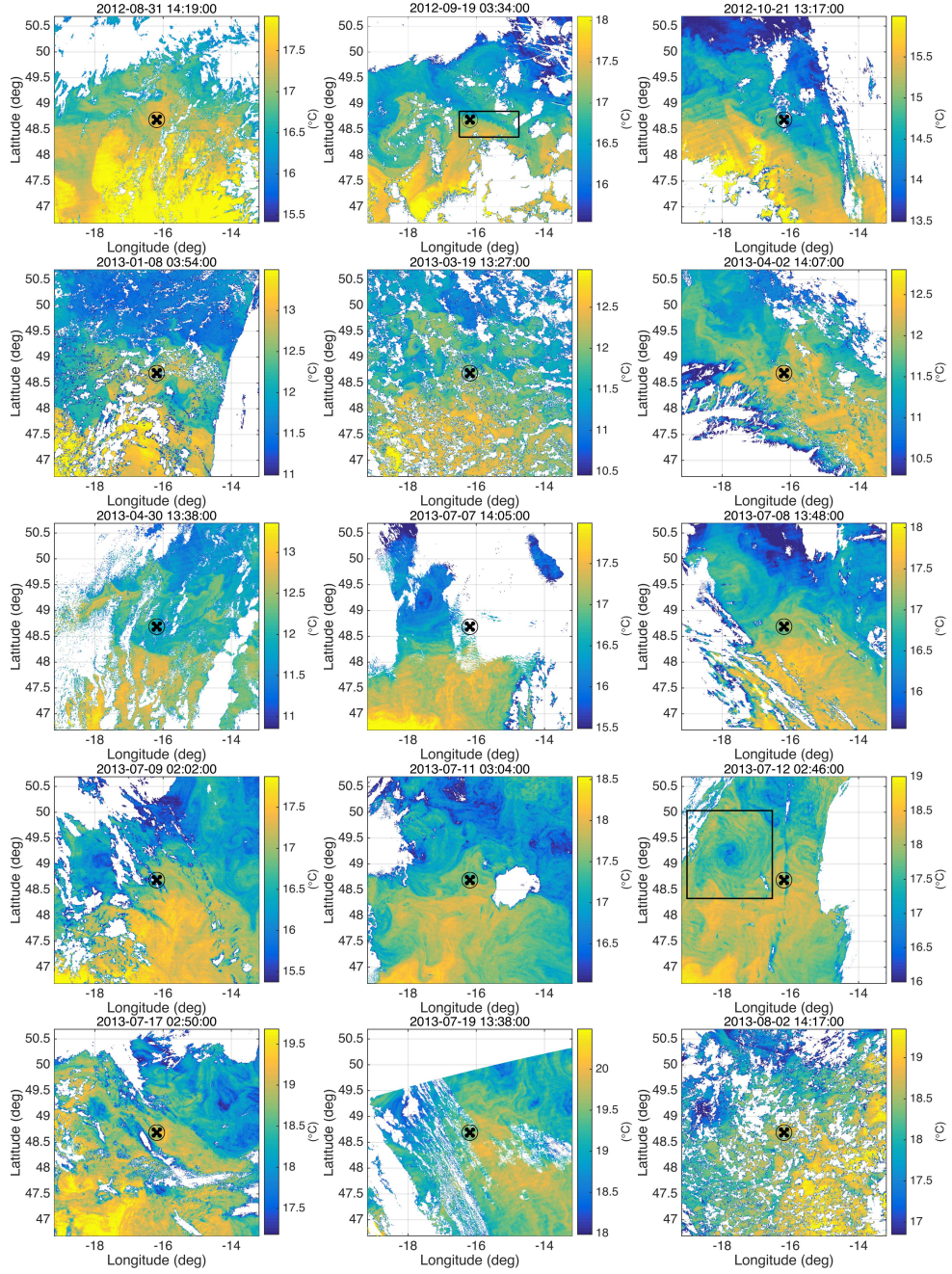


Figure 1. SST from Visible and Infrared Imaging Radiometer Suite (VIIRS) during September 2012–September 2013. The circles ($R_1 = 17$ km) circumscribing the asterisks indicate the OSMOSIS observation location. Note: VIIRS SST indicate an unstable thermal front on 19 September 2012, 03:34 UTC (top panel, black box), and which we examine in this study (see Figure 3c of the manuscript). Also note: an anticyclonic mesoscale eddy is observed immediately west of the observation location, for example, on 12 July 2013 at 02:46 UTC. The decrease in temperatures compared to surrounding waters suggests upwelling of cool, nutrient-rich waters, a process attributed to symmetric instability by *Brannigan* [2016].

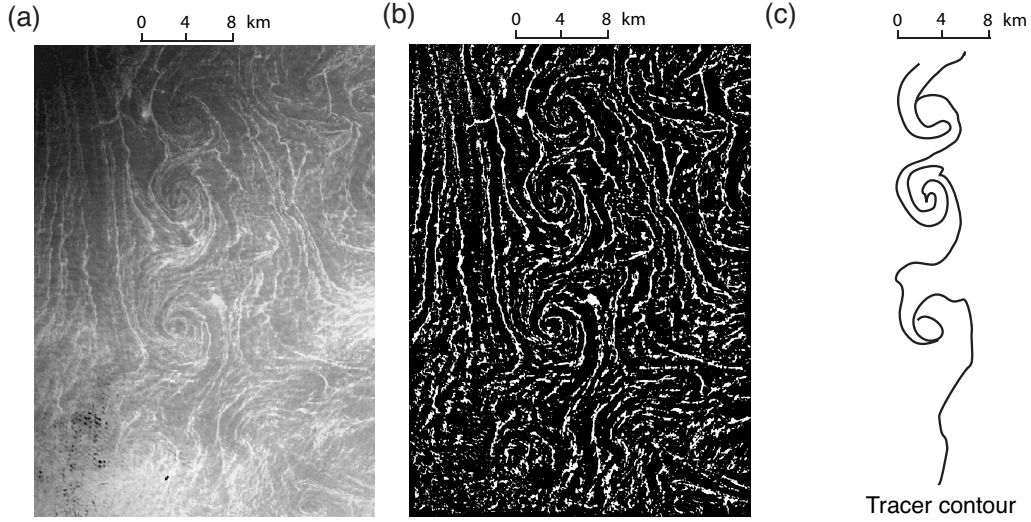


Figure 2. (a) Optical image of the ocean surface from the Apollo spacecraft mission, 7 October 1984, STS41G-35-94. (reproduced from *Munk et al.* [2000] with permission from The Royal Society). (b) Binary image after normalization and morphological operations [*Gonzalez et al.*, 2004]. (c) Tracer contour drawn by the author using the binary image shown in (b). The tracer contour has an appearance similar to the passive tracer contour (i.e., SST) documented within this study.

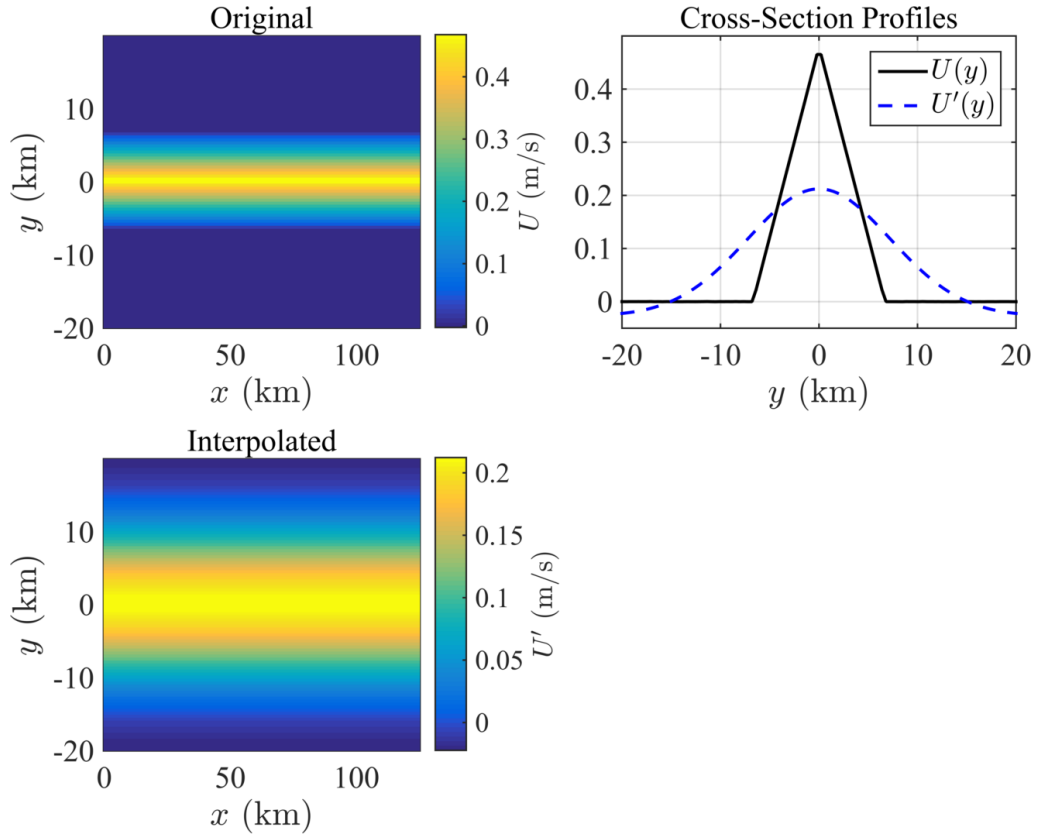


Figure 3. Result of applying the Barnes analysis to a simulated jet: (a) original jet-like velocity field, $U(y)$, (b) jet-like velocity field after optimal interpolation, $U'(y)$, and (c) comparison of zonally-averaged profiles, $U(y)$ and $U'(y)$.

